

The Tidal Origin of the Environment Dependence of Halo Assembly

Oliver Hahn^{1*}, Cristiano Porciani¹, Avishai Dekel² and C. Marcella Carollo¹

¹*Department of Physics, ETH Zürich, 8093 Zürich, Switzerland*

²*Racah Institute of Physics, The Hebrew University, Jerusalem 91904, Israel*

Accepted ???. Received ???; in original form ???

ABSTRACT

We uncover the origin of the puzzling anti-correlation between the formation epoch of galactic dark-matter haloes and their environment density. This correlation has been revealed from cosmological N -body simulations and it is in conflict with the simple excursion-set model of halo clustering. Using similar simulations, we first quantify the straightforward association of an early formation epoch with a reduced mass growth rate at late times. We then find that the primary driver of suppressed growth, by accretion or mergers, is tidal effects dominated by a neighbouring massive halo. The tidal effects range from a slowdown of the assembly of haloes due to the shear along the large-scale filaments that feed the massive halo to actual mass loss in haloes that pass through the massive halo. Our results suggest that the dependence of formation epoch on environment density is a secondary effect induced by the enhanced density of haloes in filaments near massive haloes where the tides are strong. Our measures of assembly rate are particularly correlated with the tidal field at high redshifts $z \sim 1$.

Key words: cosmology: theory, dark matter, large-scale structure of Universe – galaxies: formation, haloes – methods: N -body simulations

1 INTRODUCTION

Dark-matter haloes provide the gravitational potential wells in which galaxies form, and as such, the understanding of their assembly process during the cosmological history is a key element in the theory of galaxy formation. Focusing on gravitational physics while avoiding the complications associated with baryonic physics, the study of the growth of dark-matter haloes is the straightforward, more solid part of the theory of galaxy formation. The process of bottom-up assembly of dark haloes is described successfully by an approximate formalism, the Extended Press-Schechter (EPS) or excursion-set model, which combines the statistics of an initial Gaussian random fluctuation field with the gravitational instability theory of linear fluctuation growth and with the non-linear spherical collapse model (Bond et al. 1991; Lacey & Cole 1993). In the simplest version of this model, the assembly history of a halo is predicted to be fully determined by its mass, independently of its environment (e.g. Bardeen et al. 1986; Efstathiou et al. 1988; Mo & White 1996). More sophisticated versions of EPS do involve a certain environment dependence, but they do not recover the correlation seen in the simulations (Catelan et al. 1998; Taruya & Suto 2000). The mere mass dependence, motivated by the simplest EPS model, lies at the basis of the widely used scheme for galaxy clustering that utilises the Halo Occupation Distribution (HOD) (see Cooray & Sheth 2002, and references therein).

However, numerical simulations of cosmological clustering

revealed that the halo assembly history does depend on the density of haloes in its environment (Sheth & Tormen 2004; Gao et al. 2005; Wechsler et al. 2006; Harker et al. 2006; Hahn et al. 2007; Gao & White 2007; Croton et al. 2007). For example, when the halo history is parameterised by a formation redshift z_{form} corresponding to the time by which the halo had assembled one half of its current mass, haloes that formed earlier are found to be more strongly clustered and, equivalently, reside in denser environments. This effect is valid for haloes that are much smaller than the current characteristic gravitationally collapsing mass-scale $M_* \sim 10^{13} M_{\odot}$ (at redshift zero). The origin of this and related deviations from the predictions of EPS, sometimes termed “assembly bias” (Gao & White 2007), is not obvious — it poses a very interesting open theoretical question which deserves a simple understanding.

There have been several incomplete attempts to understand the assembly bias. Sandvik et al. (2007) noted that the assembly bias can be incorporated in an excursion-set scenario where the spherical collapse model is replaced by ellipsoidal collapse and the density threshold for halo collapse depends on the shape and size of the local environment. Another model for the incorporation of environmental effects into the excursion-set model has been discussed by Desjacques (2007). A physical explanation of this ad-hoc environmental dependence is still lacking.

In another attempt, Wang et al. (2007) found that small old haloes tend to reside next to very massive haloes. Considering the velocity dispersion of the dark-matter flow in the immediate vicinity of massive haloes they found that this velocity dispersion is higher for older haloes. They suggested that the accretion onto a

* E-mail: hahn@phys.ethz.ch

halo is suppressed once the environmental velocity dispersion exceeds the halo’s virial velocity. This scenario assumes that the dark-matter fluid is “hotter” in regions of higher density, and that the halo environment exceeds the halo virial temperature (see also Mo et al. 2005). This is difficult to reconcile with the finding that the dark-matter flow in dense filaments is rather “cold” (e.g. Klypin et al. 2003).

In this article, we address the hypothesis that the early formation times of haloes of a given mass much below the non-linear mass in dense environments are primarily driven by the *tidal* suppression of the halo growth rate in the vicinity of a neighbouring massive halo. Small, typical (low-sigma) halos tend to form in filaments (e.g. Porciani et al. 2002a), and stream along them into more massive, rare (high-sigma) haloes. The tidal field in these regions is likely to generate a shear flow and suppress the halo growth by accretion or mergers. This suppression is expected to be correlated with the proximity to the massive halo. Those small haloes that have already passed through the inner regions of bigger haloes are likely to have lost mass due to tidal stripping (Gill et al. 2005; Diemand et al. 2007; Ludlow et al. 2008) and thus show the earliest formation times.

In order to test this hypothesis, we quantify in several different ways the halo assembly history and its environment, and study the correlations between the adopted quantities. The traditional parameterisation of assembly history via the formation epoch z_{form} is complemented with more direct measures of halo growth rate at different redshifts. The environment, commonly referred to by the halo number density or the two-point correlation function, is characterised instead by the tidal/shear field, via the eigenvalues of the deformation tensor. The correlations between assembly history and environment are shown graphically and measured via a correlation coefficient. The primary role of the tidal field over the density field is to be addressed by the relative strength of the corresponding correlations with the assembly history.

The outline of this article is as follows. In Section 2, we summarise the specifics of our N -body simulations and the dark-matter halo catalogues. In Section 3, we recover the dependence of halo formation times on environment density and clustering amplitude. In Section 4 we introduce further measures of halo assembly complementing formation redshift. In Section 5, we define the relevant characteristics of the tidal field and illustrate their relation to mass assembly. In Section 6, we demonstrate the tidal origin of assembly bias, by quantifying the correlation between the tidal field and the assembly rate, and comparing it to the correlation with environment density. We discuss our analysis in Section 7 and provide our conclusions in Section 8.

2 NUMERICAL SIMULATIONS

2.1 Specifics of the N -body simulations

We use a series of three high-resolution cosmological N -body simulations that were obtained with the tree-PM code GADGET-2 (Springel 2005). These simulations are used to follow the non-linear evolution of density perturbations in a flat Λ CDM cosmology with a matter density parameter $\Omega_m = 0.25$, baryonic contribution $\Omega_b = 0.045$, and a present-day value of the Hubble constant $H_0 = 100 h \text{ km s}^{-1}$ with $h = 0.73$. The initial power spectrum has a long-wave spectral index of $n = 1$, and is normalised so that the RMS fluctuation within a sphere of $8 h^{-1} \text{ Mpc}$ linearly extrapolated to the present time is $\sigma_8 = 0.9$. Each of the three simulations

follows 512^3 collisionless dark matter particles in periodic boxes of sizes 45, 90 and $180 h^{-1} \text{ Mpc}$, respectively. Initial conditions were generated using the GRAFIC tool (Bertschinger 2001) at $z \simeq 79, 65$ and 52 for the three boxes. The corresponding particle masses are $4.7 \times 10^7, 3.8 \times 10^8$ and $3.0 \times 10^9 h^{-1} M_\odot$, respectively. Particle positions and velocities were saved for 30 time-steps, logarithmically spaced in expansion parameter a between $z = 10$ and $z = 0$. Unless otherwise stated, data from the simulation with the highest mass resolution, the $45 h^{-1} \text{ Mpc}$ box, is used for the analysis of the lowest mass haloes. Results have been checked for resolution effects against the other boxes.

2.2 Identification of haloes and the properties of their assembly

We identify bound structures using the standard friends-of-friends (FOF) algorithm (Davis et al. 1985) with a linking length equal to 0.2 times the mean inter-particle distance. Among all these dark-matter haloes, we keep only those haloes at $z = 0$ that fulfil the virialization constraint $|2T/V + 1| < 0.5$ where T is the kinetic energy and V is the potential energy of the group of particles. In addition, we also exclude those groups where the most-bound particle is further than $R_{\text{max}}/4$ away from the centre of mass, where R_{max} is the distance of the furthest FOF particle from the group’s centre of mass.

For each halo at redshift $z = 0$ we find its progenitors at any desired redshift $z > 0$ by identifying all the haloes that have particles in common with the final halo. At each snapshot, the most massive progenitor that contributes at least half of its particles to the final halo at $z = 0$ is identified as the “main progenitor”. We define the formation redshift z_{form} of a halo of mass M_0 at $z = 0$ as the redshift at which a main progenitor with mass $M \geq M_0/2$ first appears in the simulation. The “assembly history” of a halo, for our current purpose, is simply the mass-growth history of its main progenitor, $M(z)$.

In addition, we say that a halo underwent a “mass-loss” event if between any successive snapshots along its history it contributed at least 3% of its mass to a more massive halo that is not a main progenitor of the same final halo.¹

3 THE DEPENDENCE OF FORMATION TIME ON ENVIRONMENT

The assembly bias has been detected using measures of either environment density or halo clustering. We first confirm these findings using our simulations.

3.1 Dependence on Environmental Density

At a fixed halo mass, the assembly bias can be measured as a systematic trend of halo formation time with the local density of the environment (e.g. Harker et al. 2006). We estimate the density at halo positions by smoothing the distribution of N -body particles on a given scale by convolving the particle positions with a spherical top-hat kernel of radius R . In practice, we first compute the density on a Cartesian grid using cloud-in-cell interpolation and then perform the convolution with the kernel using FFT. We denote with the

¹ According to equation (4) this is equivalent to a ~ 5 per cent change in measured formation redshift.

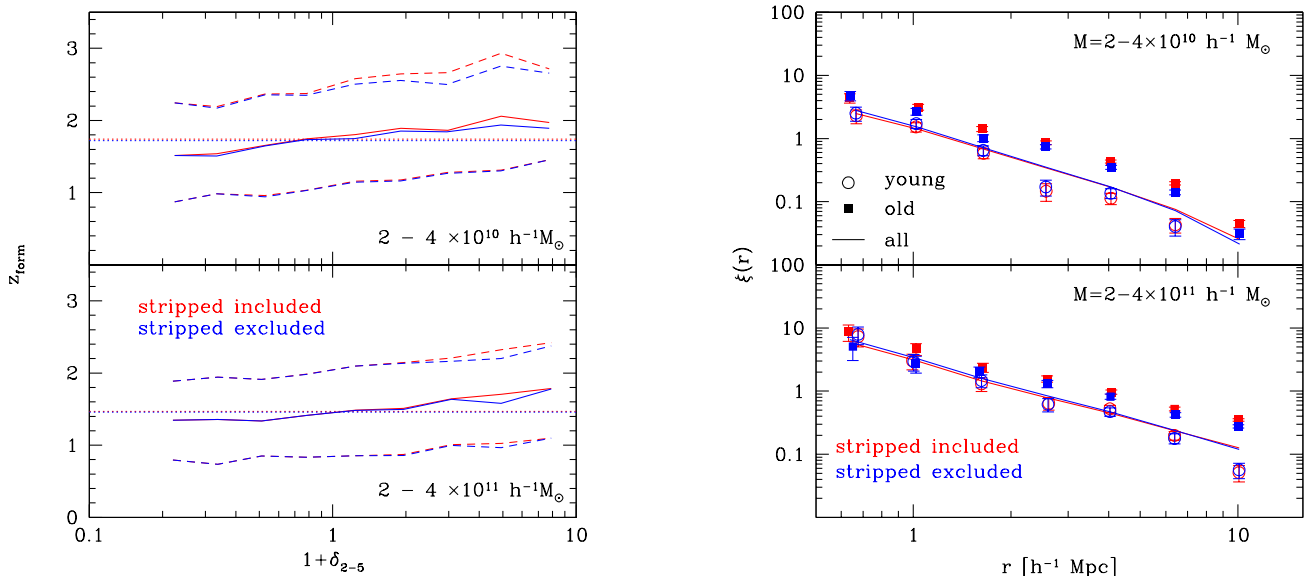


Figure 1. (Left Panel): Median formation redshift (solid line) as a function of the overdensity δ_{2-5} (see text for explanation) for all haloes, including those that experienced tidal mass loss (red), and only those haloes that never underwent such a mass loss (blue). The dashed lines indicate the 16th and 84th percentile in each bin. Results are shown for two different mass-ranges, indicated in the respective panels. The dotted lines show the median formation redshift for each sample. (Right Panel): Two-point correlation functions for all haloes (solid lines), and for those haloes of given mass that have 20 per cent highest/lowest formation times (filled squares/open circles). All results are shown including those haloes that experience tidal stripping of their mass (red) and excluding them (blue). See Section 2.2 for the definition of tidally stripped haloes.

symbol δ_R the mass overdensity computed using a smoothing radius of $R h^{-1} \text{Mpc}$. Similarly, we call $\delta_{R_1-R_2}$ the overdensity computed within a spherical shell with an inner radius of $R_1 h^{-1} \text{Mpc}$ and an outer radius of $R_2 h^{-1} \text{Mpc}$.

Figure 1 (left panel) shows the median and $\pm 1\sigma$ percentiles of z_f as a function of δ_{2-5} for our simulated haloes in two mass bins. We recover the trend found by Harker et al. (2006), and extend it to lower masses. We note that the removal of mass-losing haloes from the sample makes a difference preferentially at high densities and at the high end of the z_f distribution. We will return to these haloes in Section 6.3 where we quantify their abundance.

3.2 Dependence on Clustering Amplitude

Alternatively, the assembly bias can be discussed in terms of the halo clustering amplitude. The 2-point correlation function $\xi(r)$ is defined as the excess probability (with respect to random) to find two haloes in volume elements dV_1 and dV_2 separated by a comoving distance r ,

$$dP_{12}(r) \equiv \bar{n}^2 [1 + \xi(r)] dV_1 dV_2, \quad (1)$$

where \bar{n} indicates the mean halo number density. The assembly bias has been originally seen as a systematic dependence of the amplitude of $\xi(r)$ with halo formation time (Gao et al. 2005; Gao & White 2007). At constant halo mass, older haloes tend to be more strongly clustered than younger ones. The age dependence of the clustering amplitude is evident only for haloes with mass $M < M_*(z)$. Here $M_*(z)$ denotes the mass scale for which 1σ density fluctuations typically collapse at redshift z according to the Press-Schechter model. The linear rms overdensity on this mass scale has then to be $\sigma(M_*(z), z) = \delta_c \simeq 1.686$. At all redshifts, the number density of haloes with $M > M_*(z)$ is exponentially

suppressed. In Figure 1 (right panel) we show how $\xi(r)$ changes with halo age in our simulations. The ratio of the different correlation functions agrees very well with the results of Gao & White (2007) and extends the analysis also to lower masses.

4 HALO MASS ASSEMBLY HISTORIES

In this section we introduce measures of halo assembly complementing the common parameterisation of assembly histories through the formation time.

4.1 The mass assembly rate of haloes

We define the current assembly rate of each halo by taking the time derivative of its smoothed assembly history $\mathcal{S}[M(z)]$, where \mathcal{S} is some smoothing operation. From the smoothed assembly histories, we define the current assembly rate as (cf. Neistein et al. 2006)

$$A(z) \equiv -\frac{d}{dz} \ln \mathcal{S}[M(z)]. \quad (2)$$

Smoothing by local regression with a window of 0.5 in redshift proved to be well suited and has been used in our analysis. It is necessary to smooth since the assembly histories of single haloes are prone to fluctuations that are due to the intrinsic stochasticity of the simulation/halo-identification process.

In close analogy to the definition of the formation redshift, we will use the ratio $G(z) \equiv M(0)/M(z)$ between the final mass and the mass at redshift z as the “forward” measure of halo growth since redshift z .

Both quantities $A(z)$ and $G(z)$ are strongly related with the integral measure z_{form} (note that $G(z_{\text{form}}) = 1/2$ by definition of z_{form}). In Table 1 we show the Spearman rank correlations between

ρ_s	$z = 0$	$z = 0.5$	$z = 1$	$z = 2$
$M(0) = 2 - 4 \times 10^{10} h^{-1} M_\odot$				
$(z_{\text{form}}, A(z))$	-0.58	-0.62	-0.65	-0.08
$(z_{\text{form}}, G(z))$	-	-0.40	-0.67	-0.87
$(A(z), G(z))$	-	0.42	0.32	0.16
$M(0) = 2 - 4 \times 10^{11} h^{-1} M_\odot$				
$(z_{\text{form}}, A(z))$	-0.46	-0.57	-0.29	0.50
$(z_{\text{form}}, G(z))$	-	-0.40	-0.77	-0.81
$(A(z), G(z))$	-	0.36	-0.03	-0.30

Table 1. Spearman rank correlation coefficients ρ_s between three different measures of halo mass assembly: the formation redshift z_{form} , the assembly rate $A(z)$ and the mass growth ratio $G(z)$. The coefficients are given for the progenitors of haloes identified at $z = 0$ with masses between 2 and $4 \times 10^{10} h^{-1} M_\odot$ (top) in the $45 h^{-1} \text{Mpc}$ box, and for haloes with masses between 2 and $4 \times 10^{11} h^{-1} M_\odot$ (bottom) in the $90 h^{-1} \text{Mpc}$ box.

these different measures as a function of redshift for the main progenitors of haloes with masses between 2 and 4×10^{10} and 2 and $4 \times 10^{11} h^{-1} M_\odot$ at $z = 0$. The median formation redshift for the first sample of haloes is 1.71 while it is 1.44 for the latter. We use the rank correlation coefficient rather than the linear Pearson correlation coefficient as it does not assume a linear relation between the correlated quantities.

For haloes of a given mass at $z = 0$, a large (small) $G(z)$ at high redshift implies trivially that the main progenitor mass was already high (low) at that epoch so that its formation time is high (low). The progenitor then also has a high (low) assembly rate $A(z)$ at early times and a low (high) $A(z)$ at late times.

Thus, a high formation redshift is related to a low assembly rate $A(z)$ at late times ($z \lesssim z_{\text{form}}$) and a high assembly rate at early times ($z \gtrsim z_{\text{form}}$). The latter can be seen for the higher mass sample where the median formation redshift is sufficiently low so that the correlation coefficient changes sign at $z = 2$. At late times, the formation redshift depends most sensitively on the assembly rate around $0.5 \lesssim z \lesssim 1$ for the low mass sample and around $z \sim 0.5$ for the higher mass sample.

4.2 The influence of mass loss on formation time

While typical analytic models of structure formation predict a monotonous growth of halo mass over time, haloes do undergo interactions with other haloes which can lead to tidal mass-loss. The influence of such a mass-loss event on the measured formation time of a halo can be estimated as follows. Several studies of structure formation in a bottom-up scenario (e.g. van den Bosch 2002; Wechsler et al. 2002) have suggested that the bulk of haloes assembles the mass exponentially with redshift:

$$M(z) = M(0) \exp(-\alpha z) \quad (3)$$

where α is the mass-assembly rate. In this case, $z_{\text{form}} = \alpha^{-1} \log 2$. Let us assume that the smooth mass accretion history is interrupted at redshift z_{loss} by a single mass loss of $M_{\text{loss}} \equiv x M(z_{\text{loss}})$. For simplicity, the growth rate α is assumed to be identical before and after z_{loss} (it is trivial to extend our results to the most general case). A short calculation shows that mass loss leads to an increase in measured formation redshift given by

$$z_{\text{form}} = \frac{1}{\alpha} \ln \frac{2}{1-x}. \quad (4)$$

5 THE EFFECT OF TIDAL FORCES ON THE ASSEMBLY OF HALO MASS

In this section we will demonstrate that the proximity to a massive halo provides a special environment for the formation and evolution of lower-mass haloes due to tidally sheared flows influencing their assembly.

5.1 Halo evolution in the proximity to a massive halo

For a large number of haloes in our simulation, we investigated the evolution of their Lagrangian patches and of their Lagrangian environments. At all epochs, the Lagrangian patch of a halo is defined by the set of particles that are identified as part of the halo at $z = 0$. Similarly, we define the Lagrangian environment as the set of particles that in the initial conditions of the simulations were lying within a cube of $3h^{-1} \text{Mpc}$ centred on the corresponding Lagrangian patch. We observe significant differences between old and young haloes of a given mass.

The older haloes are very likely found in pronounced large-scale structure already at high redshifts, while this is not true for the younger haloes. In Figure 2 we show the evolution of the particles making up two different haloes at $z = 0$ together with their Lagrangian environment. One of the haloes has a very high formation redshift of $z_{\text{form}} = 3.1$ while the other halo has a low formation redshift of $z_{\text{form}} = 0.42$. It is evident from the evolution of the environment of the old halo that, once the host filament formed, its neighbouring haloes show an expanding, ‘‘Hubble-like’’, motion along the filament, which is not present for the younger halo. In the rest-frame of the halo this expansion along the filament appears as a recession of the neighbouring haloes in that direction. Remarkably, in both cases, the last major merger occurs perpendicular to the host large-scale structure. Thus, the gravitational shear accelerates the collapse perpendicular to the filament while it slows down the collapse along the filament (cf. Porciani et al. 2002a,b). Tidal forces are expected to increase substantially in the vicinity of very massive haloes leading to a strong correlation between the tidal field and the density field on larger scales. This leads to the correlation of halo properties that are influenced by the external tidal field with the density field.

5.2 Quantifying tidally sheared flows

The dynamics of dark-matter flows (and thus the accretion onto dark-matter haloes) is regulated by the gradient of the gravitational potential $\nabla\phi$ and the tidal tensor

$$T_{ij} = \left[\frac{\partial^2}{\partial_i \partial_j} - \frac{1}{3} \delta_{ij} \nabla^2 \right] \phi, \quad (5)$$

where δ_{ij} denotes the Kronecker symbol. The presence of a massive halo that locally dominates the gravitational potential generates a strong tidal field in its neighbourhood. Over time, the tidal field produces a tidally induced shear in the velocity field of the surrounding particles. The flow is stretched in the direction of the massive halo and compressed in the plane perpendicular to it. This impacts the mass accretion history of smaller haloes neighbouring the massive one. To probe the influence of these tidal forces, we quantify the velocity field surrounding small-mass haloes by expanding the local (peculiar) flow with respect to the bulk motion of the halo up to linear order

$$v_i = \frac{\partial v_i}{\partial x_j} x_j. \quad (6)$$

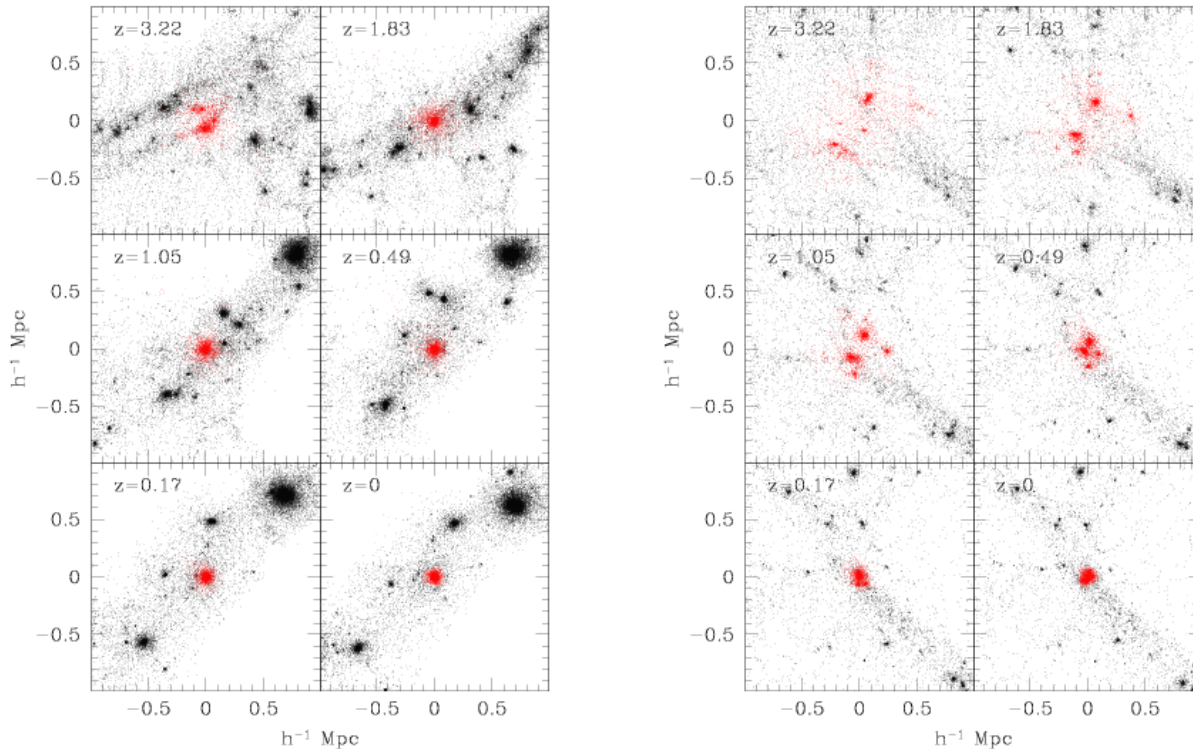


Figure 2. Evolution of the patch of two haloes with mass $1.4 \times 10^{11} h^{-1} M_{\odot}$ at $z = 0$ and formation redshift $z_{\text{form}} = 3.1$ (left) and $z_{\text{form}} = 0.42$ (right). Particles that will constitute the halo at $z = 0$ are shown in red while particles that are contained in a $3 h^{-1} \text{Mpc}$ cube centred on the Lagrangian patch are shown in black. The centre of the coordinate system moves with the centre of mass of the particles that constitute the halo at $z = 0$.

We next perform a least squares fit of the nine components of the velocity gradient tensor within one and four virial radii around each halo (cf. Porciani et al. 2002a,b). It is then possible to write the velocity gradient tensor as the sum of a symmetric and an antisymmetric part

$$\begin{aligned} \frac{\partial v_i}{\partial x_j} &= \frac{1}{2} \left(\frac{\partial v_i}{\partial x_j} + \frac{\partial v_j}{\partial x_i} \right) + \frac{1}{2} \left(\frac{\partial v_i}{\partial x_j} - \frac{\partial v_j}{\partial x_i} \right) \\ &\equiv D_{ij} + \Omega_{ij}, \end{aligned} \quad (7)$$

where D_{ij} corresponds to the rate-of-strain tensor, and Ω_{ij} describes rigid rotation due to nonzero vorticity $\omega_i \equiv (\nabla \times \mathbf{v})_i = -\epsilon_{ijk} \Omega_{jk}$, where ϵ_{ijk} is the Levi-Civita symbol. The rate-of-strain tensor can be further decomposed as $D_{ij} \equiv \theta \delta_{ij} + \Sigma_{ij}$ where θ denotes the velocity divergence (or expansion scalar) and Σ_{ij} is the traceless shear tensor with eigenvalues $\mu_1 \leq \mu_2 \leq \mu_3$. For growing-mode fluctuations in the linear regime, $T_{ij} \propto \Sigma_{ij}$ and therefore the eigenvectors of these matrices are aligned. However, the proportionality of the shear and tide is broken by higher-order terms. In general, the eigenvectors of the tensors remain parallel but the eigenvalues evolve differently with time (e.g. Bertschinger & Jain 1994). In fact, while tides act as sources for the velocity shear, the latter is also influenced by the velocity gradient, vorticity and the shear itself. In what follows, we use the velocity shear as a measure of the integrated effect of the gravitational tides.

Both random motion and nonlinear ordered motion will be superimposed onto the ordered deformation so that we can define a velocity dispersion along the three main axes of the rate-of-strain

tensor quantifying this residual by

$$\sigma_i^2 \equiv \langle ((\mathbf{v} - \lambda_i \mathbf{x} - \boldsymbol{\omega} \times \mathbf{x}) \cdot \mathbf{w}_i)^2 \rangle, \quad (9)$$

where $\lambda_1 \leq \lambda_2 \leq \lambda_3$ are the eigenvalues and \mathbf{w}_i are the corresponding eigenvectors of the rate-of-strain tensor D_{ij} . Furthermore we define a simple relative velocity \mathbf{v}_{rel} between a halo's centre of mass velocity and the mean velocity of the region between one and four virial radii. If the velocity field is completely linear then both $|\mathbf{v}_{\text{rel}}| = 0$ and $|\boldsymbol{\sigma}| = 0$. We observe that, apart from very little scatter, $|\boldsymbol{\sigma}|$ is completely dominated by $|\mathbf{v}_{\text{rel}}|$. Nonzero $|\boldsymbol{\sigma}|$ and $|\mathbf{v}_{\text{rel}}|$ can arise when the velocity grows non-linearly with distance from the halo, due to the presence of other haloes within 1–4 virial radii or in special circumstances when the halo has indeed a relative velocity with respect to its surrounding flow. We will return to this last aspect in Section 6.3. Furthermore, $|\boldsymbol{\sigma}|$ will also reflect resolution effects that impact the goodness of the linear fit to the flow.

5.3 The shear flow near early forming haloes

In Figure 3, we show the cumulative distribution functions of the eigenvalues μ_i of the traceless shear tensor Σ_{ij} for haloes with highest and lowest assembly rates A at $z = 0.5$, where the effect is strongest. The joint distribution of the eigenvalues is known analytically for a Gaussian random field (cf. Doroshkevich 1970). We observe a systematic trend of μ_3 towards more positive and of μ_1 towards more negative values for those haloes that grow slower. This implies that the flow around these haloes is more strongly sheared. Sheared motion in the flow provides clear evidence for the presence

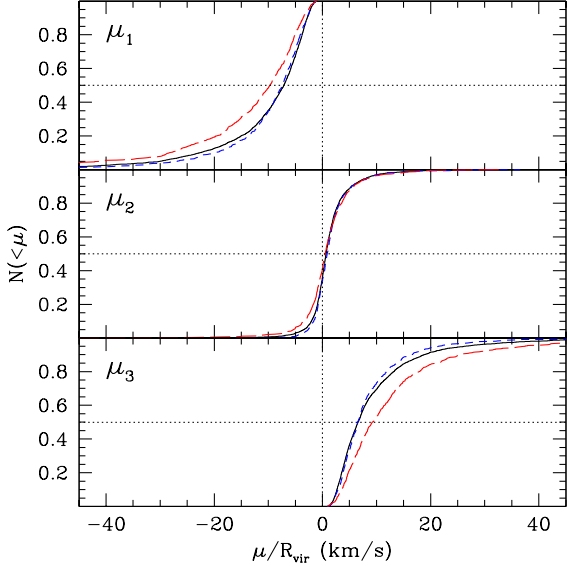


Figure 3. Cumulative distribution functions of the eigenvalues μ_i of the shear tensor Σ_{ij} . The data is shown for the $z = 0.5$ progenitors of haloes with masses between 2×10^{10} and $4 \times 10^{10} h^{-1} M_\odot$ at $z = 0$. Lines correspond to all these haloes (solid, black), those 20 per cent with highest current assembly rate (short dashes, blue) and those with the lowest (long dashes, red). Stripped haloes are excluded.

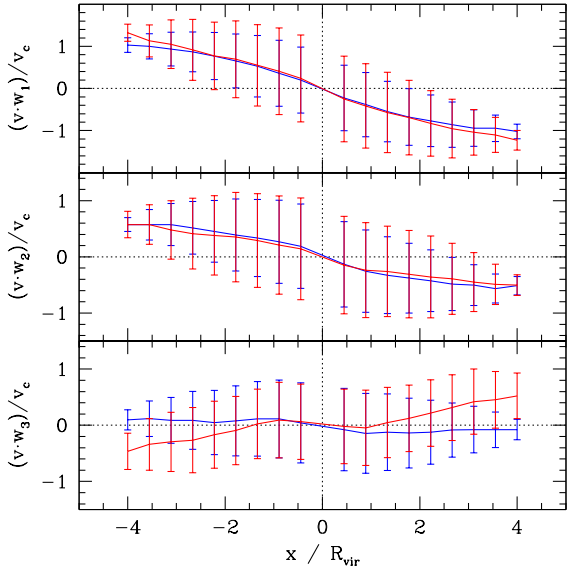


Figure 4. Median velocity field along the three main axes of the rate-of-strain tensor \mathbf{w}_1 (top), \mathbf{w}_2 (middle) and \mathbf{w}_3 (bottom). The data is shown for the $z = 1$ progenitors of haloes with masses between 2×10^{10} and $4 \times 10^{10} h^{-1} M_\odot$ at $z = 0$. The sample of haloes is split into those 20 per cent with largest (blue) and smallest (red) increase in mass. Stripped haloes are excluded. Errorbars correspond to the medians of the 16th and 84th percentiles for each halo.

of an external tidal field. Such an effect occurs e.g. for haloes near a big neighbouring halo, where the accretion is suppressed along the radius vector from the centre of the big halo.

In Figure 4 we show the median velocity of the environment as a function of distance from the halo centre projected along the three main axes of the rate-of-strain tensor (which are equivalent to the main axes of the shear tensor). Results are shown for haloes growing most and least in mass between redshift one and zero for the progenitors of haloes of fixed mass at $z = 0$. While the flow fields are comparable along \mathbf{w}_1 and \mathbf{w}_2 apart from slightly larger scatter for the less growing haloes, we find a large qualitative difference along the eigenvector \mathbf{w}_3 corresponding to the largest eigenvalue λ_3 . Along this direction matter is receding from the halo centre leading to a Hubble-like flow that counteracts infall onto the halo. The data is shown at $z = 1$ where the difference in the flow field is strongest when splitting the halo sample in growth $G(z)$.

6 THE TIDAL ORIGIN OF THE ASSEMBLY BIAS

The hierarchical structure-formation picture based on the Extended Press-Schechter model (Lacey & Cole 1993) predicts that the mass of the main progenitor of a halo is determined by the sequence of “density peaks” on increasingly larger scales that exceed the threshold for collapse. In this picture, all properties depend only on the halo mass without any influence of the environment.

We will show in this section that this simple picture is found to be violated in our N -body simulations and the assembly behaviour of haloes is modulated by tidal effects ranging from the suppression of halo growth to tidal mass loss due to an encounter with a massive halo in the most extreme cases.

6.1 The influence of tides on halo mass assembly

In order to quantify the interplay between environment and halo mass assembly, we present Spearman rank correlation coefficients between measures of environment and measures of halo mass assembly in Tables 2 and 3 at four redshifts for the main progenitors of haloes identified at $z = 0$. In Table 2 data is shown for haloes in the $45 h^{-1} \text{Mpc}$ simulation with masses between 2 and $4 \times 10^{10} h^{-1} M_\odot$ at $z = 0$. Table 3 shows the corresponding data for haloes with masses between 2 and $4 \times 10^{11} h^{-1} M_\odot$ at $z = 0$ from the $90 h^{-1} \text{Mpc}$ simulation.

We find that for both mass ranges the correlation of formation redshift and the eigenvalue λ_3 is strongest at redshifts close to the median formation redshift of the sample. Furthermore, the correlation of assembly rate $A(z)$ with λ_3 increases between redshifts 2 and 0.5 and is significantly stronger for the lower mass sample. Finally, we find that at all redshifts a large λ_3 is related to a small growth $G(z)$ and vice versa.

The correlations with λ_3 can now be compared with the dependence of assembly on environment density. At all redshifts above zero, the correlation coefficients between the overdensity in spheres of $2 h^{-1} \text{Mpc}$ and the three measures of mass assembly are significantly weaker than those with λ_3 . Most remarkably, the correlation between δ_2 and z_{form} is strongest at $z \sim 1 - 2$, the epoch where however z_{form} correlates significantly stronger with λ_3 indicating that the density itself is not the primary cause for the suppression.

In Figure 5 we show graphically the correlations between λ_3 and δ_2 on the one hand and $A(z)$, $G(z)$ and z_{form} on the other hand. In all cases, at fixed A , G or z_{form} , the scatter in density

ρ_s	$z = 0$	$z = 0.5$	$z = 1$	$z = 2$
$(z_{\text{form}}, \lambda_3(z))$	0.11	0.22	0.30	0.25
$(z_{\text{form}}, \delta_2(z))$	0.15	0.17	0.19	0.21
$(z_{\text{form}}, \delta_S(z))$	0.15	0.06	-0.08	-0.23
$(z_{\text{form}}, \sigma(z))$	0.15	0.18	0.22	0.28
$(A(z), \lambda_3(z))$	-0.13	-0.28	-0.23	-0.14
$(A(z), \delta_2(z))$	-0.18	-0.18	-0.15	-0.07
$(A(z), \delta_S(z))$	-0.17	-0.07	0.0	0.01
$(A(z), \sigma(z))$	-0.17	-0.20	-0.14	-0.07
$(G(z), \lambda_3(z))$	-	-0.29	-0.32	-0.29
$(G(z), \delta_2(z))$	-	-0.13	-0.18	-0.20
$(G(z), \delta_S(z))$	-	0.09	0.21	0.37
$(G(z), \sigma(z))$	-	-0.19	-0.21	-0.21
$(\delta_2(z), \lambda_3(z))$	0.60	0.55	0.47	0.37
$(\delta_S(z), \lambda_3(z))$	0.59	0.53	0.46	0.28
$M_{\text{med}}(z)$	2.7	2.2	1.7	1.1

Table 2. Spearman rank correlation coefficients ρ_s between measures of halo mass assembly and measures of environment over redshift. Measures of environment are λ_3 , the largest eigenvalues of the rate-of-strain tensor, the overdensity δ_S in the shell within one and four virial radii around each halo, δ_2 the matter field smoothed with a spherical top-hat filter of scale $2 h^{-1}$ Mpc and the deviation from a linear flow $|\sigma|$. Measures of mass assembly are the formation redshift z_{form} , the assembly rate $A(z)$ and the mass ratio $G(z)$. The coefficients are given for haloes with masses between 2 and $4 \times 10^{10} h^{-1} M_{\odot}$ at $z = 0$. These haloes have a median formation redshift $z_{\text{med}} = 1.71$. The median mass $M_{\text{med}}(z)$ of the halo sample at redshift z is given in units of $10^{10} h^{-1} M_{\odot}$. Data is obtained from the $45 h^{-1}$ Mpc box. Tidally stripped haloes are excluded. These results illustrate that: (1) mass assembly is modulated by λ_3 and (2) the correlation of λ_3 with density grows over time.

ρ_s	$z = 0$	$z = 0.5$	$z = 1$	$z = 2$
$(z_{\text{form}}, \lambda_3(z))$	0.09	0.22	0.27	0.16
$(z_{\text{form}}, \delta_2(z))$	0.15	0.17	0.18	0.19
$(z_{\text{form}}, \delta_S(z))$	0.13	0.0	-0.21	-0.26
$(z_{\text{form}}, \sigma(z))$	0.11	0.13	0.17	0.30
$(A(z), \lambda_3(z))$	-0.08	-0.19	-0.08	-0.02
$(A(z), \delta_2(z))$	-0.13	-0.14	-0.07	0.08
$(A(z), \delta_S(z))$	-0.14	-0.02	-0.02	-0.09
$(A(z), \sigma(z))$	-0.12	-0.13	0.0	0.14
$(G(z), \lambda_3(z))$	-	-0.24	-0.31	-0.23
$(G(z), \delta_2(z))$	-	-0.12	-0.16	-0.19
$(G(z), \delta_S(z))$	-	0.17	0.31	0.48
$(G(z), \sigma(z))$	-	-0.11	-0.15	-0.20
$(\delta_2(z), \lambda_3(z))$	0.65	0.60	0.53	0.42
$(\delta_S(z), \lambda_3(z))$	0.52	0.46	0.32	0.12
$M_{\text{med}}(z)$	27	21	16	9.4

Table 3. Same as Table 2 but for haloes with masses between 2 and $4 \times 10^{11} h^{-1} M_{\odot}$ at $z = 0$. These haloes have a median formation redshift $z_{\text{med}} = 1.44$. Data is obtained from the $90 h^{-1}$ Mpc box.

with respect to the trend is larger than in λ_3 reflecting the stronger correlation of these quantities with λ_3 . Reduced growth is always associated with higher median λ_3 and δ_2 .

In addition, we also measured correlations with the overdensity δ_S in the shell between 1 and 4 virial radii around each halo – the region from which the halo receives the material for accretion. As expected, if the overdensity in this region is large at early times, the halo can accrete material from this region. This is reflected in an anticorrelation between δ_S and z_{form} at redshifts 1 and 2 and the positive correlation with $G(z)$.

Finally, the correlation between λ_3 and δ_2 is stronger than that with δ_S at all redshifts and especially so for the higher mass sample. This reflects the importance of the large scale density field in producing a sheared flow rather than the local scales. Naturally, the continuity of the density field implies a strong correlation between the overdensity on the two scales. As expected, the correlation between density and λ_3 grows significantly with time.

We will now briefly discuss the influence of resolution effects in the simulation on these results. Since the mass range of haloes shown in Table 3 is resolved even better in the $45 h^{-1}$ Mpc box, albeit for a much smaller sample, we cross-checked all numbers for resolution effects and found no significant deviations between the two simulations except in the role of the residuals $|\sigma|$. At all redshifts, correlations of assembly with $|\sigma|$ were weaker and those with λ_3 slightly stronger in the simulation with higher mass resolution. This is indicative of a minor resolution dependence in determining the tensor eigenvalues from the flow that results in a slight weakening of correlations with shear. Note also that results do not change significantly if haloes are selected in a fixed mass range at some redshift $z > 0$ instead of at $z = 0$ except that all correlations with $|\sigma|$ are significantly weaker at redshifts $z > 0$ again reflecting a resolution dependence of the goodness of the linear fit to the flow.

6.2 Clustering behaviour of haloes in sheared regions

Tidal fields are strongest in the vicinity of massive haloes where also the clustering of smaller haloes is substantially enhanced. In Figure 6 we show the correlation functions for haloes with the largest/smallest eigenvalue λ_3 of the rate-of-strain tensor at redshifts zero and their main progenitor haloes at redshift one. As expected, haloes at redshift zero with high λ_3 are significantly more clustered than average haloes while those with low λ_3 are less clustered. At redshift one the situation is slightly different: only haloes with highest λ_3 are significantly more clustered than average haloes. Furthermore, haloes with the lowest λ_3 show a strong attenuation of the correlation function at distances below $\sim 1 h^{-1}$ Mpc. This is a clear indication that these haloes are only found in less clustered regions. See also the discussion in Appendix A2 for the dependence of clustering amplitudes on environmental overdensity in the initial density field.

The tidal field, as quantified by the sheared flow around a halo, thus shows a strong correlation with all quantities of mass assembly as well as the dependence on clustering amplitude that is necessary to account for the halo assembly bias.

6.3 Tidal stripping of halo mass

We will now quantify the population of the most extreme examples of tidally suppressed mass assembly, those haloes that experience a tidal mass loss inside the virial radius of a more massive halo but are still identified as isolated haloes. As described in Section 4.2,

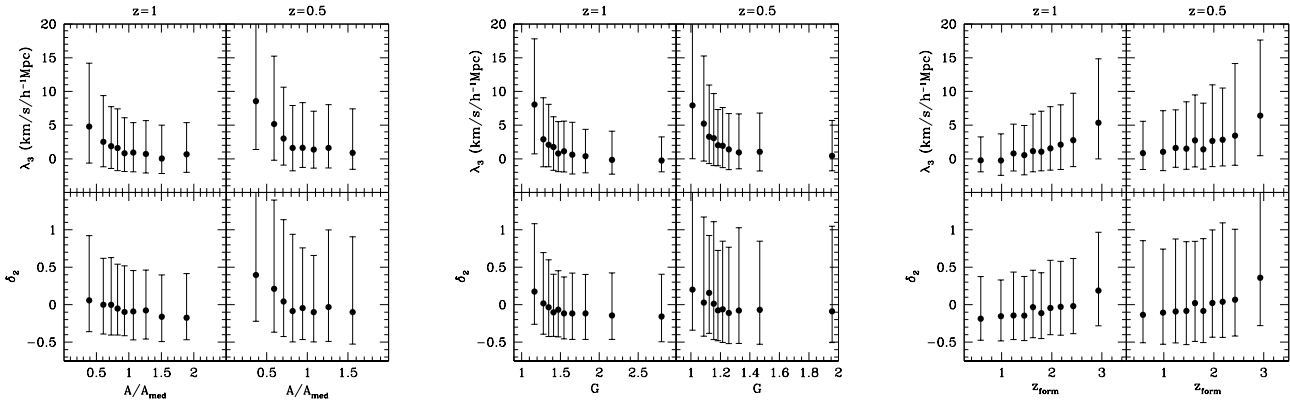


Figure 5. (Left panel): Median values of $\lambda_3(z)$ (top) and $\delta_2(z)$ (bottom) as a function of halo assembly rate $A(z)$ at $z = 1$ (left) and $z = 0.5$ (right) for haloes with masses between 2 and $4 \times 10^{10} h^{-1} M_{\odot}$ at $z = 0$. (Middle panel): Same as left panel but as a function of the mass ratio $G(z)$. (Right panel): Same as left panel but as a function of z_{form} . Errorbars correspond to the 16th and 84th percentile in each bin. Bins are chosen to include equal numbers of points. Stripped haloes are excluded.

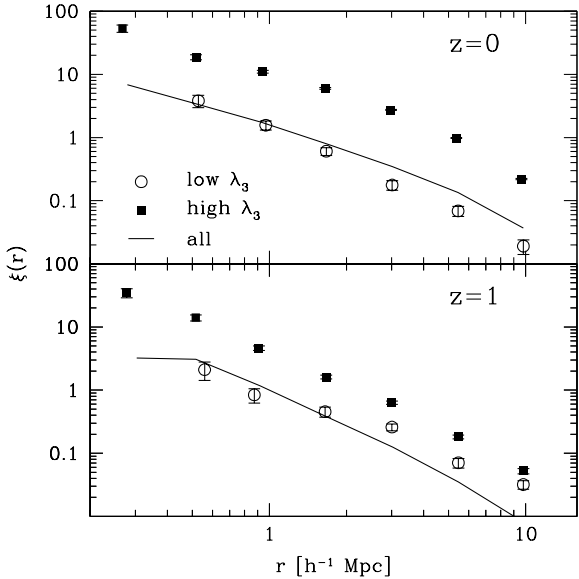


Figure 6. Two-point correlation functions for haloes with masses between 2 and 4×10^{10} at redshift zero. The two panels correspond to these haloes at redshift zero (top) and their main progenitor haloes at redshift one (bottom). The samples have been split into those haloes at the respective redshift with the 20 percent highest/lowest values in λ_3 , the largest eigenvalue of the rate-of-strain tensor. Tidally stripped haloes are not included. Haloes experiencing strong tides, as probed by λ_3 , are much stronger clustered than haloes in low shear regions.

the stripping implies an underestimation of halo mass at $z = 0$ relative to the assembly history at higher z which is equivalent to an overestimation of the formation redshift. It is thus crucial for our analysis to quantify the abundance of these objects.

In Figure 7 we show the fraction of well resolved haloes in our simulations that are found as isolated haloes at $z = 0$ and are considered as stripped according to the definition in Section 2.2. At a given mass, this fraction is on the order of a few per cent. The fraction is higher for smaller halo masses and reaches a value of ~ 4.5 per cent for $M \simeq 2 \times 10^{10} h^{-1} M_{\odot}$.

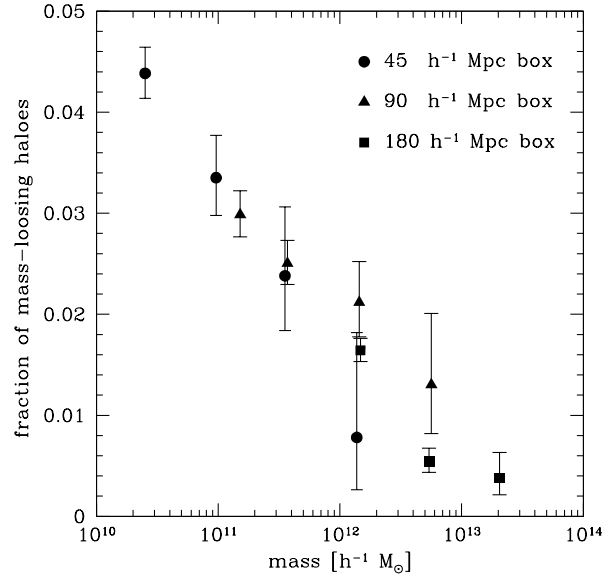


Figure 7. Fraction of haloes losing at least 3 per cent of their mass to a more massive halo as a function of halo mass at redshift $z=0$. Errorbars indicate the 1σ Poisson uncertainties. Results are shown for the three simulations of different resolution described in the text. At a given mass, only few per cent of haloes have undergone tidal mass-loss to a larger halo.

These tidally stripped haloes certainly contribute to establishing the assembly bias but cannot fully explain it by themselves. Rather they should be considered as the most extreme case of tidally suppressed mass growth. In Figure 1 (left panel) we showed how the correlation of formation redshift with overdensity δ_{2-5} changes when the haloes that lost mass due to an encounter with a more massive object are removed from the sample. The population of stripped haloes consists mainly of outliers more than 1σ away from the median of the non-stripped population. Removing them lowers the median formation redshift of haloes in regions of high density. However, since the stripped haloes make up only a small fraction of the population, we still observe a significant dependence of halo formation redshift on environmental density that

is less severely affected by tides. In addition, in the right panel of Figure 1 the corresponding effect is also shown for the two-point correlation function. As for the correlation with density, removing the tidally stripped haloes has some effect by decreasing the clustering of the oldest haloes. However, also for the correlation function analysis a remaining age-dependent bias persists.

Furthermore, haloes that are at the apocenter of their orbit after passing through a massive halo are also likely to have very large relative velocities with respect to their environment. Considering the relative velocity between a halo and the surrounding region within 1 and $4 R_{\text{vir}}$ (cf. Section 5.3), we find that haloes identified as stripped haloes indeed show large relative velocities with respect to their environment. These relative velocities will lead to extreme velocity dispersions around haloes and are possibly dominating the results of Wang et al. (2007). These authors attribute the measured velocity dispersion to random motion while, however, also relative motion with respect to a bulk flow and a strongly sheared flow will lead to an increase in velocity dispersion. When removing the stripped haloes, we find that the correlation between relative velocity and formation redshift weakens substantially.

7 DISCUSSION

The formation redshift of dark-matter haloes is highest for haloes that have the lowest assembly rate at late times (cf. Section 4.1). Tying this suppression of late growth to a physical effect that is most effective in dense/strongly clustered regions will thus explain the correlation of halo clustering and formation redshift, the so-called “assembly bias”.

Tidal forces induce a sheared flow in the vicinity of small haloes that flow along filaments of the cosmic web (Section 5.1). To quantify this effect, we measured the local influence of the larger scale tidal field by considering the rate-of-strain tensor of the flow in the immediate vicinity of haloes. We found that the progenitors of haloes of a given mass at $z = 0$ that experience the strongest shear in their history have significantly lower assembly rates than haloes in less strongly sheared regions.

Tidal effects are expected to be strongest close to massive haloes. Given that a mass M at distance r completely dominates the potential, the tide in the direction of this mass is given by $2GM/r^3$, while the perpendicular tides are given by $-GM/r^3$. In the restframe of the smaller halo, matter is receding along the direction to the massive halo. Furthermore, upon approaching the massive halo, the environment density will grow substantially and as a consequence the correlation between density and shear grows with time (see Section 6). Since the abundance of small haloes is enhanced near massive haloes, the population of tidally suppressed haloes will be biased such that a dependence of formation redshift on clustering amplitude and environment density arises as a secondary effect. The more fundamental character of tides is reflected in the stronger correlation of measures of halo growth with λ_3 than with environment density (Section 6).

In the most extreme cases, small haloes can undergo tidal mass-loss when passing through the massive halo. A minor fraction of haloes of a given mass are indeed not typical isolated haloes since they are once again found outside the virial radius of a massive halo after their first pericenter passage through its potential well. These haloes have also been observed in resimulations of single massive haloes (Gill et al. 2005; Diemand et al. 2007; Ludlow et al. 2008). Our results, however, demonstrate that this population of tidally stripped haloes is small and represents

only the most extreme examples of tidal influence on halo mass assembly (c.f. Section 6.3).

Tidal suppression of halo growth seems to be already present in the quasi-linear regime. Keselman & Nusser (2007) recover the assembly bias also using the punctuated Zel’dovich approximation where the mass of haloes grows monotonously by definition and tidal mass-loss is impossible.

We explore the link between assembly bias and the initial linear density field in Appendix A where we compare the masses of haloes measured from the simulations with the masses they should reach in an isolated environment according to the EPS model. Our results indicate that the EPS predicted masses are roughly a factor of 2-3 higher for the oldest haloes than for the youngest. Furthermore, we find a significant correlation between this mismatch and both the strength of the shear and large scale density at $z = 0$ in the simulation. This provides further evidence that indeed the environment, that is not considered when determining the EPS-like masses, prevents the mass to grow to the predicted value. Hence, while EPS would predict that the halo will assemble mass, the strong shear that EPS does not account for prevents this (see also van de Weygaert & Babul 1994). If the correct final mass is known, it can be shown that the density dependence of formation redshifts can be reproduced using a simple peak-background-split model (see Appendix A).

A question that is opened by our analysis is whether the last major merger of small haloes occurs preferentially perpendicular to their host filament such that the mechanism we described is potentially also related to alignments between halo spins and shapes and the surrounding large-scale structure. For small galactic dark matter haloes such strong alignments between halo shape and the direction to the nearby cluster have been found by Pereira et al. (2008) extending out to many virial radii of the cluster and by alignments of both halo shape and spin with host filaments and sheets by Hahn et al. (2007) and Aragón-Calvo et al. (2007) (see also Basilakos et al. (2006) and Ragone-Figueroa & Plionis (2007)). Lee & Erdogdu (2007) found observational evidence for an alignment of galaxy spins with the reconstructed tidal field. In the picture outlined in this paper, the decreased probability for mergers or accretion along the filament would preserve the spin vector alignment with the filament/sheet which is established when merging occurs preferentially perpendicular to the filament/sheet.

8 SUMMARY AND CONCLUSIONS

Using a series of cosmological N -body simulations, we demonstrated that the mass assembly of haloes is substantially influenced by tidal effects in the vicinity of massive haloes. The resulting suppression of mass growth at late times is reflected in an increase in formation redshift. The space density of small haloes near massive haloes is enhanced. Thus, as a secondary effect, a tidally suppressed assembly of halo mass directly translates into biased spatial distributions of young and old haloes identified at $z = 0$: old haloes will be found more likely in regions of high density than younger haloes.

The presence of tides changes the infall behaviour onto a halo. To quantify this, we measured the influence of external tides by considering the rate-of-strain tensor, and especially its largest eigenvalue λ_3 , fitted to the flow between 1 and 4 virial radii around haloes. This gives a good indication of linearly sheared flows. In detail, we found that for small haloes:

- (i) High formation redshift is related to a low assembly rate at

late times. Thus any spatially biased process that suppresses mass growth at late times can potentially lead to an age dependent bias of halo clustering.

(ii) Among all measures of environment that we considered, assembly rate at redshifts $z > 0$ correlates most strongly with the largest eigenvalue λ_3 of the rate-of-strain tensor, and especially so when measured at high redshift, $z \sim 1$. The correlation of assembly rate with the density of the environment is weaker. We find that haloes with a low assembly rate have suppressed infall or even outflow in the region between 1 and 4 virial radii along one direction.

(iii) The correlation between λ_3 (probing shear and tides) and density grows with time, so that haloes in strongly sheared regions are much more strongly clustered than average and associated with high density regions. Hence the suppression of infall is stronger in regions of high density.

(iv) The value of λ_3 of a given halo at high redshift is a good predictor of the final halo mass at $z = 0$.

(v) There is a small fraction of haloes that experience tidal mass-loss to a more massive halo while orbiting through its virial radius. These haloes are the most extreme cases of tidal suppression and cannot account alone for the observed assembly bias.

(vi) The mismatch between the mass that the Extended Press-Schechter formalism would attribute to a halo and the mass that is measured for it in the simulation correlates with formation time and with the eigenvalue λ_3 indicating a dependence of this mismatch on tides.

From the evidence presented above, we conclude that the tidal field due to neighbouring massive haloes exerts a shear on the flow surrounding small haloes. In the rest-frame of the small halo, this is an outward flow along the direction to the more massive halo, tidally suppressing the growth of the small halo. This is especially effective in filaments since most of the matter is located along the direction from which it is least effective for the halo to accrete.

The necessary proximity to more massive haloes, where the clustering of haloes is enhanced, leads to a spatial bias of haloes experiencing strong tides and thus also to a bias of the population of “old” and “young” haloes of the same mass. We conclude that this is the origin of the *assembly bias*.

ACKNOWLEDGEMENTS

OH acknowledges support from the Swiss National Science Foundation. CP thanks the participants of the Aspen workshop “Modelling Galaxy Clustering” for discussions. AD’s research has been supported by GIF I-895-207.7/2005, by the Einstein Center at HU, by NASA ATP NAG5-8218, and by a French-Israel cooperation program. All simulations were performed on the Gonzales cluster at ETH Zürich, Switzerland.

REFERENCES

Aragón-Calvo M. A., van de Weygaert R., Jones B. J. T., van der Hulst J. M., 2007, *ApJ*, 655, L5
 Bardeen J. M., Bond J. R., Kaiser N., Szalay A. S., 1986, *ApJ*, 304, 15
 Basilakos S., Plionis M., Yepes G., Gottlöber S., Turchaninov V., 2006, *MNRAS*, 365, 539
 Bertschinger E., 2001, *ApJS*, 137, 1
 Bertschinger E., Jain B., 1994, *ApJ*, 431, 486
 Bond J. R., Cole S., Efstathiou G., Kaiser N., 1991, *ApJ*, 379, 440

Catelan P., Lucchin F., Matarrese S., Porciani C., 1998, *MNRAS*, 297, 692
 Cooray A., Sheth R., 2002, *Phys. Rep.*, 372, 1
 Croton D. J., Gao L., White S. D. M., 2007, *MNRAS*, 374, 1303
 Davis M., Efstathiou G., Frenk C. S., White S. D. M., 1985, *ApJ*, 292, 371
 Desjacques V., 2007, *arXiv:0707.4670*, 707
 Diemand J., Kuhlen M., Madau P., 2007, *ApJ*, 667, 859
 Doroshkevich A. G., 1970, *Astrophysics*, 6, 320
 Efstathiou G., Frenk C. S., White S. D. M., Davis M., 1988, *MNRAS*, 235, 715
 Gao L., Springel V., White S. D. M., 2005, *MNRAS*, 363, L66
 Gao L., White S. D. M., 2007, *MNRAS*, 377, L5
 Gill S. P. D., Knebe A., Gibson B. K., 2005, *MNRAS*, 356, 1327
 Hahn O., Carollo C. M., Porciani C., Dekel A., 2007, *MNRAS*, 381, 41
 Hahn O., Porciani C., Carollo C. M., Dekel A., 2007, *MNRAS*, 375, 489
 Harker G., Cole S., Helly J., Frenk C., Jenkins A., 2006, *MNRAS*, 367, 1039
 Keselman J. A., Nusser A., 2007, *MNRAS*, 382, 1853
 Klypin A., Hoffman Y., Kravtsov A. V., Gottlöber S., 2003, *ApJ*, 596, 19
 Lacey C., Cole S., 1993, *MNRAS*, 262, 627
 Lee J., Erdogdu P., 2007, *ApJ*, 671, 1248
 Ludlow A. D., Navarro J. F., Springel V., Jenkins A., Frenk C. S., Helmi A., 2008, *arXiv: astro-ph/0801.1127*
 Mo H. J., White S. D. M., 1996, *MNRAS*, 282, 347
 Mo H. J., Yang X., van den Bosch F. C., Katz N., 2005, *MNRAS*, 363, 1155
 Neistein E., van den Bosch F. C., Dekel A., 2006, *MNRAS*, 372, 933
 Pereira M. J., Bryan G. L., Gill S. P. D., 2008, *ApJ*, 672, 825
 Porciani C., Dekel A., Hoffman Y., 2002a, *MNRAS*, 332, 325
 Porciani C., Dekel A., Hoffman Y., 2002b, *MNRAS*, 332, 339
 Ragone-Figueroa C., Plionis M., 2007, *MNRAS*, 377, 1785
 Sandvik H. B., Möller O., Lee J., White S. D. M., 2007, *MNRAS*
 Sheth R. K., Tormen G., 2004, *MNRAS*, 350, 1385
 Springel V., 2005, *MNRAS*, 364, 1105
 Taruya A., Suto Y., 2000, *ApJ*, 542, 559
 van de Weygaert R., Babul A., 1994, *ApJ*, 425, L59
 van den Bosch F. C., 2002, *MNRAS*, 331, 98
 Wang H. Y., Mo H. J., Jing Y. P., 2007, *MNRAS*, 375, 633
 Wechsler R. H., Bullock J. S., Primack J. R., Kravtsov A. V., Dekel A., 2002, *ApJ*, 568, 52
 Wechsler R. H., Zentner A. R., Bullock J. S., Kravtsov A. V., Allgood B., 2006, *ApJ*, 652, 71
 Zel’dovich Y. B., 1970, *A&A*, 5, 84

APPENDIX A: ASSEMBLY BIAS IN THE INITIAL DENSITY FIELD

A1 Predicting the assembly bias from the initial density field

Can we predict the amplitude of the assembly bias directly from the linear density field? This requires being able to forecast the formation redshift, final mass and local Eulerian density of a halo directly from the initial conditions.

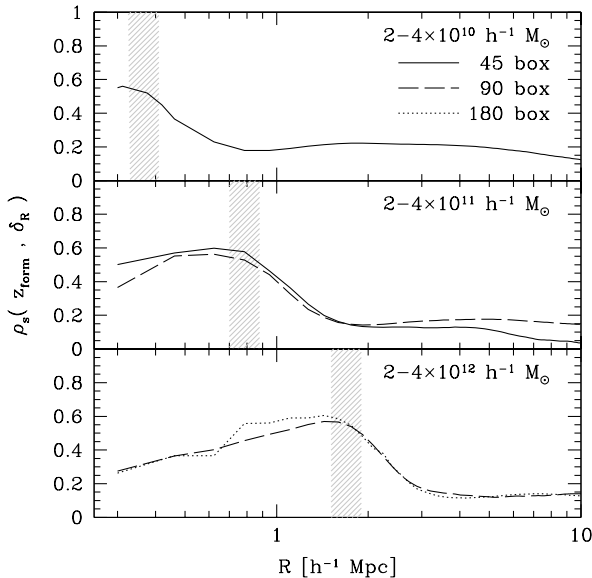


Figure A1. Spearman rank correlation coefficient ρ_s between halo formation redshift z_{form} and “peak height” of the Lagrangian density field smoothed with a real space top hat filter on scale R as a function of the filter scale. Results are shown for three mass ranges. Results for the different simulations are indicated by different line styles. The shaded regions indicate the half-mass range $M/2$ for the corresponding mass bins. This analysis reveals: (1) The correlation coefficient peaks as expected for haloes of mass M on scales around $M/2$; and (2) the correlation with the large scale density field on several $h^{-1}\text{Mpc}$ is significant.

A1.1 Halo formation redshift

What determines the formation redshift of a halo? In Figure A1, we show the Spearman rank correlation coefficient between the formation redshift z_{form} and the linear overdensity field evaluated at the centre of mass of the Lagrangian patch that will form a halo at $z = 0$. The overdensity field is computed after smoothing the density field with a top-hat filter of radius R . The rank correlation coefficients with z_{form} are plotted against R . Our results show that the formation time of a halo of mass M is most strongly determined by the value of the linear overdensity smoothed on a scale $\sim M/2$. This is what one trivially expects for spherical perturbations. Tides on slightly larger scales (but still internal to the protohalo) also correlate with z_{form} but to a lesser degree (not shown in the figure). The tidal suppression of halo assembly discussed in the previous sections manifests itself in the initial condition as a residual correlation between z_{form} and δ_R for large smoothing scales. The rank correlation coefficient is as high as 0.2 even for smoothing radii of a few Mpc. The presence of nearby density fluctuations influences the formation time of a given halo. In other words, contrary to the Press-Schechter ansatz, the collapse of a perturbation on a given scale depends on the presence of density fluctuations with larger wavelength.

A1.2 The assembly bias

If the final halo masses are known, the assembly bias can be perfectly reproduced starting from the initial density field and using a simple peak-background split model where small-scale fluctua-

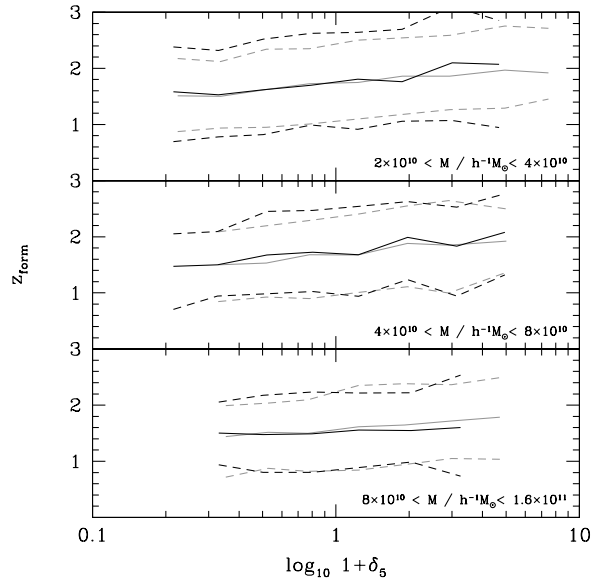


Figure A2. Halo formation time as a function of environmental density on scales $5h^{-1}\text{Mpc}$ obtained from the N -body simulations (grey) and obtained from the initial conditions data using a combination of two spherical collapse models for the evolution of the background and the peak (black), the mass of the halo is taken from the N -body simulation. Stripped haloes are not considered. Solid lines indicate the median, dashed lines the $\pm 1\sigma$ spread around the median.

tions are responsible for halo collapse and large-scale fluctuations determine the local density of the halo environment.

Inspired by Figure A1, we assume that the formation redshift \hat{z}_{form} of a halo of mass M is fully determined by the “peak height” $\delta_{M/2}$. Denoting by $D_+(z)$ the linear growth factor of density fluctuations, we thus solve the condition for collapse of a spherical density perturbation

$$\frac{D_+(\hat{z}_{\text{form}})}{D_+(z_i)} \delta_{M/2} = \delta_c, \quad (\text{A1})$$

where z_i is the initial redshift. We find that a value of $\delta_c = 2.3$ leads to the best agreement between \hat{z}_{form} and z_{form} obtained from the N -body simulation.

In a second step, we determine the evolution of the background density field δ_5 on scales of $R_b = 5h^{-1}\text{Mpc}$. Small haloes that survive until $z = 0$ will preferentially form in regions that are underdense on these scales in the initial density field. They will then migrate into regions of higher density over time. We determine the evolution of the background density using first-order Lagrangian perturbation theory. Given the eigenvalues λ_i of the initial tidal field on scales of $R_{b,0}$, the evolution of δ_5 at the positions of the haloes is given by

$$\delta_b(z) = \frac{1}{\prod_{i=1}^3 [1 - D_+(z) \lambda_i]} - 1 \quad (\text{A2})$$

in the Zel’dovich approximation (Zel’dovich 1970).

For each halo in the N -body simulation, we thus obtain an environmental density at $z = 0$ and the redshift of collapse \hat{z}_{form} by knowing a priori its final mass and its Lagrangian position. In Figure A2 we show the median formation redshift \hat{z}_{form} (in grey) as a function of density δ_5 for three mass bins. The corresponding relation is shown also for the quantities directly obtained from the

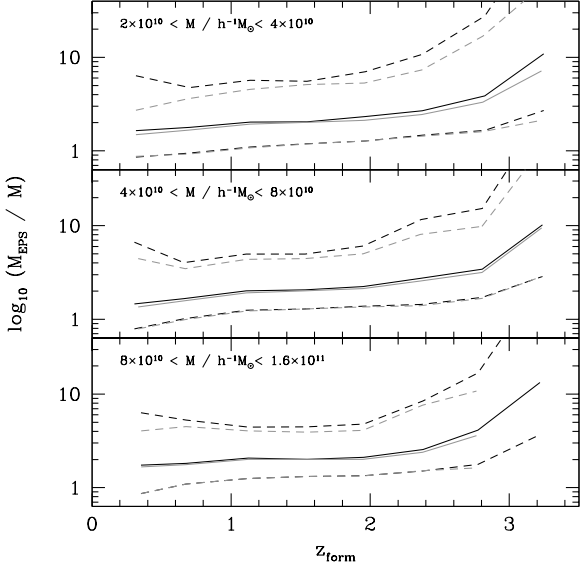


Figure A3. The ratio of mass determined in the initial conditions to mass measured in the N -body simulation as a function of halo formation time. Solid lines indicate the median, dashed lines the 1σ spread around the median. Shown is the relation for haloes that are not undergoing tidal mass-loss (grey) and for all haloes (black) in three mass bins.

N -body simulation (in black). We find very good agreement between the two corresponding relations such that our results suggest that this simple model suffices to predict the correlation between formation redshift and environment seen in the simulations.

Replacing the actual halo masses with those predicted at the Lagrangian halo locations by the Extended Press-Schechter (EPS) formalism is sufficient to completely erase any dependence of the formation redshift on environmental density. The spherical collapse model (on which the EPS method is based) tends to overestimate halo masses, particularly for those haloes that are located within strongly sheared flows. In Figure A3 we show how the formation redshift z_{form} depends on the ratio between the mass M_{EPS} and the mass M , where z_{form} and M are determined from the N -body simulations. We find that the mismatch increases from a median ratio of about 1.5 at low formation redshifts to about 3 at high formation redshifts for the considered masses (cf. Figure 3 in Wang et al. 2007). When we exclude the mass-stripped haloes (grey lines) the scatter is significantly reduced. The ratio between the EPS-predicted mass and the mass found in the N -body simulations correlates with the largest eigenvalue λ_3 of the rate-of-strain tensor as strongly as with the halo formation redshift. For haloes at $z = 0$ with masses between 2 and $4 \times 10^{10} h^{-1} M_{\odot}$ the Spearman rank correlation coefficient between M_{EPS}/M and the shear eigenvalue λ_3 is 0.29. It is 0.27 between M_{EPS}/M and z_{form} . This provides further evidence that tidally suppressed accretion is responsible for the existence of the assembly bias. The proximity to a massive halo is reflected in the correlation coefficient with density obtained with the top-hat filter at $z=0$. We find that the coefficient with M_{EPS}/M is 0.22 for density determined on scales of $5 h^{-1} \text{Mpc}$, 0.31 for $2 h^{-1} \text{Mpc}$ and 0.41 for $0.5 h^{-1} \text{Mpc}$.

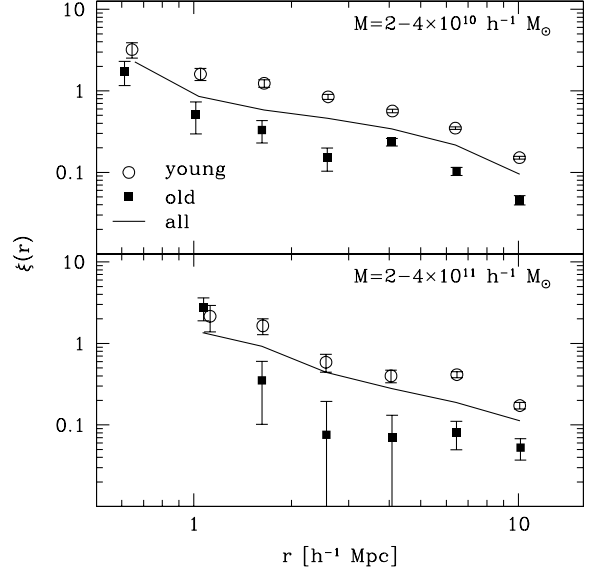


Figure A4. Two-point correlation functions of the Lagrangian centres of mass in the initial density field ($z = 78.5$) for haloes with masses $2 - 4 \times 10^{10} h^{-1} M_{\odot}$ at $z = 0$ (upper panel) and $2 - 4 \times 10^{11} h^{-1} M_{\odot}$ (lower panel). The solid line shows the correlation function for all haloes, while open circles and filled squares correspond to the 10 per cent of these haloes with lowest and highest formation redshifts, respectively.

A2 Lagrangian assembly bias

It is interesting to verify whether the assembly bias is already present in the spatial distribution of protohaloes in the linear density field. To this aim, we compute the two-point correlation of the Lagrangian patches of old and young haloes (selected at $z = 0$) at the initial redshift of our simulations.

Figure A4 shows the correlation function of the protohaloes that will form objects with masses between 2 and $4 \times 10^{10} h^{-1} M_{\odot}$ at $z = 0$.

The corresponding correlations at $z = 0$ have been presented in Figure 1. At $z = 0$ the oldest haloes cluster more strongly than the youngest ones. For the Lagrangian patches, however, the opposite is true: the oldest (youngest) haloes are significantly less (more) clustered than the total. This indicates that, already in the linear density field, the environments surrounding the Lagrangian patches of young and old haloes have different properties. In particular, we find that both young and old haloes at these masses form in initially underdense (i.e. with a median $\delta_5 < 0$) regions. However, the Lagrangian patches of young protohaloes reside (on average) in more underdense regions which, in a Gaussian random field, are more strongly clustered. Using the mean squared overdensities at the halo centres as a proxy for their clustering amplitude (i.e. assuming a linear bias model independent of halo age for the halo density), $B = \langle \delta_5^2 \rangle^{1/2}$, we find $B_{\text{old}}/B_{\text{all}} = 0.8$ and $B_{\text{young}}/B_{\text{all}} = 1.2$. On the other hand, with time, the protohaloes will collapse and flow towards denser regions thus changing their clustering properties. At $z = 0$ we find $B_{\text{old}}/B_{\text{all}} = 1.8$ and $B_{\text{young}}/B_{\text{all}} = 0.33$. The reversal of the assembly bias is then a simple result of the evolution of the halo environmental density. Older haloes have thus always resided in more overdense regions than younger haloes.